# Towards high-sensitivity magnetometry with nitrogen-vacancy centers in diamond using the singlet infrared absorption

Ali Tayefeh Younesi,[1] Muhib Omar,[2,3] Arne Wickenbrock,[2,3] Dmitry Budker,[2,3,4] and Ronald Ulbricht[1,*]

[1] *Max-Planck Institut für Polymerforschung, Ackermannweg 10, Mainz 55128, Germany*
[2] *Helmholtz-Institut Mainz, GSI Helmholtzzentrum für Schwerionenforschung GmbH, Mainz 55128, Germany*
[3] *Johannes Gutenberg-University Mainz, 55128 Mainz, Germany*
[4] *Department of Physics, University of California, Berkeley, California 94720-300, USA*

(Received 30 October 2024; revised 3 February 2025; accepted 31 March 2025; published 7 May 2025; corrected 26 November 2025)

The negatively charged nitrogen vacancy center in diamond is widely used for quantum sensing due to the sensitivity of the spin triplet in the electronic ground state to external perturbations such as strain and electromagnetic fields, which makes it an excellent probe for changes in these perturbations. The spin state can be measured through optically detected magnetic resonance, which is most commonly achieved by detecting the photoluminescence after exciting the spin-triplet transition. Recently, methods have been proposed and demonstrated that use the absorption of the infrared singlet transition at 1042 nm instead. These methods, however, require cryogenic temperatures or external cavities to enhance the absorption signal. Here, we report on our efforts to optimize the magnetometer sensitivity at room temperature and without cavities. We reach a sensitivity of 18 pT/$\sqrt{\text{Hz}}$, surpassing previously reported values, and a calculated shot-noise limit of 5 pT/$\sqrt{\text{Hz}}$ . We also report on a defect that is native to diamond grown by chemical vapor deposition and thus absent in high-pressure high-temperature diamond, the excitation of which impacts the measured singlet absorption signal.

DOI: 10.1103/PhysRevApplied.23.054019

## I. INTRODUCTION

The negatively charged nitrogen-vacancy (N-$V^-$) center in diamond is the most popular example of a new class of defects in solid-state crystals that promises novel applications in quantum information and metrology [1,2], as well as magnetic [3,4], electric [5–7], strain [8,9], and temperature [10,11] sensing. Among them, due to promising improvements in both sensitivity and spatial resolution besides their robustness, wide operation temperature range, and small size, N-$V$-based magnetometers have found numerous applications in condensed matter physics [12], neuroscience and living systems biology [13], nuclear magnetic resonance [14], and Earth and planetary science [15].

The N-$V^-$ center features a spin-triplet $^3A_2$ electronic ground state that can be manipulated with microwave (MW) radiation and read out through optical excitation as optically detected magnetic resonance (ODMR) [16]. The utility of N-$V^-$ for harnessing coherent spin dynamics relies on the reproducible polarization of this spin state through optical pumping, which is the result of a series of radiative and nonradiative electronic transitions that are shown in Fig. 1(a). After photoexcitation into the spin-triplet excited state $^3E$, vibrational relaxation occurs within less than 100 fs [17]. Further electronic relaxation takes place either via radiative recombination back to the $^3A_2$ state within 10 ns or via intersystem crossing (ISC) to the $^1A_1$ spin singlet. The latter transition is more probable from the spin projections states $m_s = \pm 1$ of $^3E$ compared to $m_s = 0$; see Appendix C for more details [1]. Subsequently, the electron relaxes to the $^1E$ spin-singlet state within about 100 ps [18], from where it transitions back to the $^3A_2$ state via ISC within 200 ns at room temperature [19,20]. Spin selectivity of this cycle not only leads to preferential population of $m_s = 0$ in $^3A_2$ in the absence of external perturbations (spin polarization), but also allows $m_s$ to be read out optically (ODMR). MW radiation (or other controlled perturbations such as magnetic field) is used to manipulate the spin-projection states in $^3A_2$ which are eventually measured optically.

Commonly, ODMR is performed by detecting the photoluminescence (PL) of the $^3E \rightarrow {}^3A_2$ transition, where a decrease in PL originates from a greater probability of relaxation via the ISC, which in turn is a result of a larger

*Contact author: ulbricht@mpip-mainz.mpg.de

$m_s = \pm 1$ population in the $^3A_2$ state. The $^1A_1 \rightarrow {}^1E$ singlet transition could also be used for ODMR. In that case, the $m_s = \pm 1$ population will be correlated with its PL count [21]. The PL yield of the singlet transition is, however, many orders of magnitude smaller than that of the triplet transition [22–24] due to dominant nonradiative recombination with a relaxation time of about 100 ps, which is much faster than the radiative decay channel [18]. The singlet PL is thus not an ideal signal for ODMR. The long lifetime of the $^1E$ state (around 200 ns), however, suggests that absorption from $^1E \rightarrow {}^1A_1$, instead of PL from $^1A_1 \rightarrow {}^1E$, is a viable probe for ODMR. In this case, a probe beam with a photon energy that is resonant with the singlet transition would carry the absorption signal, enabling absorption ODMR [25–29].

In comparison to PL ODMR, absorption ODMR promises higher spin contrast due to the spin selectivity of the electronic states (see Appendix C). As compared to the point source emission of PL, light collection is potentially more efficient in some probe geometries such as extended waveguide structures, fibers, or cavities. The singlet absorption is also inherently insensitive to the presence of N-$V^0$.

The absorption coefficient of the singlet transition is, however, generally considered to be too low to be of practical use due to its low oscillator strength and broad linewidth at room temperature, which leads to weak absorption values [18,25,30]. Previous works that utilized the singlet absorption for ODMR have thus either operated at cryogenic temperatures [25], where the transition linewidth is narrower and peak absorption thus larger, or placed the sample in a cavity to resonantly enhance absorption [26,27]. Cavities were also used to enhance pump absorption and simultaneously perform ODMR through the detection of the modulated pump transmission [31,32].

In this paper, we revisit the idea of utilizing the singlet ($^1E \rightarrow {}^1A_1$) absorption at room temperature to optimize its performance without the aid of a cavity. Improvements compared to previous works include a longer beam propagation path, narrow spin transition linewidths, optimized probe polarization, multifrequency MW excitation, and balanced probe beam photodetection. We achieve a magnetic sensitivity of 18 pT/$\sqrt{\text{Hz}}$, which is better than previous works that utilized cavities or worked at cryogenic temperatures. Avenues to further improve the sensitivity are discussed. We also found additional absorption contributions at the probe wavelength that originate from a defect native to diamond by chemical vapor deposition (CVD).

## II. EXPERIMENTAL METHODS

A continuous-wave (CW) laser at 532 nm (Coherent Verdi) excites an ensemble of N-$V$ centers ($^3A_2 \rightarrow {}^3E$) and a CW laser at 1042 nm is used to probe the singlet transition $^1E \rightarrow {}^1A_1$. The 1042-nm beam is generated with a tunable laser (TOPTICA DL pro), which is coupled to a polarization-maintaining single- mode fiber. The exiting beam of the fiber is collimated with a parabolic collimator and split into two paths; see Fig. 1(b). One beam is directly focused on one input of the balanced photodiode (PD, Femto Messtechnik) as a reference signal and the other passes through a halfwave plate ($\lambda/2$) that rotates the polarization of the infrared (IR) beam to maximize the interaction with specific N-$V$ center orientations. It is deflected and focused with a spherical lens to a spot about 24 μm in diameter at the center of the sample.

The output of the pump laser is attenuated with a halfwave plate and a polarizer [WP1 and P in Fig. 1(b)], respectively. The beam is focused on an acousto-optic

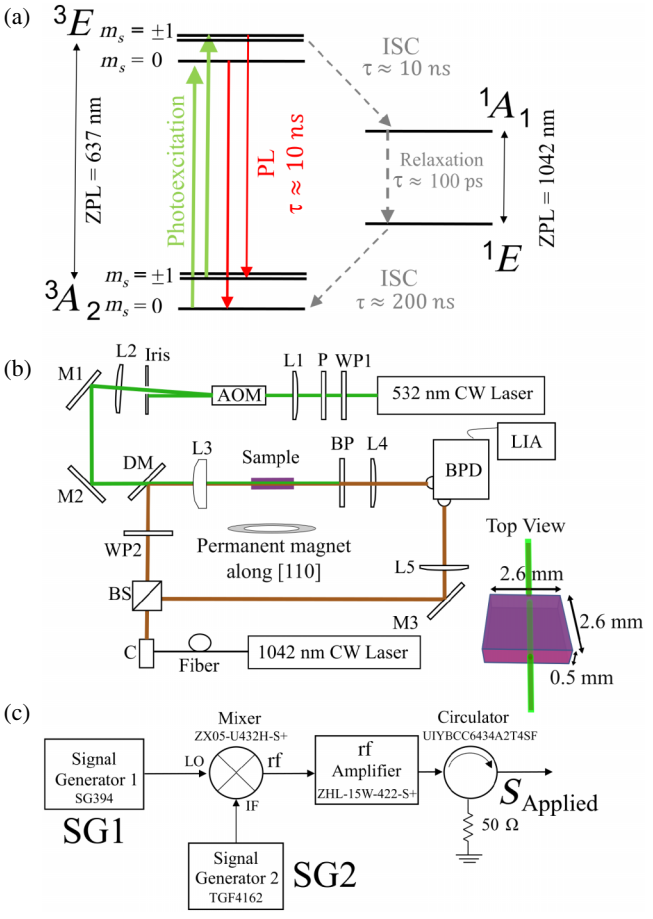


FIG. 1. (a) Electronic structure of negatively charged nitrogen vacancy (N-$V^-$) centers showing relaxation pathways and their lifetimes following photoexcitation. (b) Schematic of the setup implemented. WP, halfwave plate ($\lambda/2$); P, polarizer; L, lens; M: mirror; DM: dichroic mirror; C, collimator; BS, beam splitter; BP, bandpass filter; BPD, balanced photodetector; LIA, lock-in amplifier. (c) MW signal generation system.

modulator (AOM) (G&H 3200-146, Crystal Technology) and the first-order deflected beam is collimated with another lens (L2). The output beam is combined collinearly with the IR beam using a dichroic longpass mirror at 850 nm [DM in Fig. 1(b)], and focused with the same lens focusing the IR beam at the center of the sample that is mounted on a three-axis translation stage. The spot size of the pump at the center of the sample is around 30 μm and is assured to be larger than the IR beam over the entire sample. The Rayleigh lengths of the focused beams are calculated to be around 3 mm. The sample is a $^{12}$C-enriched CVD-grown diamond in [100] orientation, having substitutional nitrogen with a concentration of about 13 ppm (see Appendix A for more details). The N-$V$ concentration (both negatively and neutrally charged) is about 4 ppm. The sample size is $2.6 \times 2.6 \times 0.5$ mm$^3$ (polished on all six facets), and in order to have a better thermal dissipation it is placed on a bigger diamond substrate of size $60 \times 60 \times 1$ mm$^3$. To increase IR absorption, the beams pass through the long side of the sample with a length of 2.6 mm, thus increasing interaction without using a cavity. The transmitted beam is first passed through a 1040-nm bandpass filter with a full width half maximum (FWHM) of 10 nm to block the pump beam and PL generated by the sample and focused on the second input of the balanced photodiode, whose output current is amplified with a built-in amplifier. The output of the amplifier is connected to a lock-in amplifier (LIA, Zurich Instruments HF2LI), which is used to demodulate the signal at a specific frequency that is explained later.

A bias permanent magnet is placed oriented along [110] [shown in Fig. 1(b)], which has equal field strength on two N-$V$ axes ([111] and $[\bar{1}\bar{1}1]$) and is orthogonal to the other two ($[1\bar{1}\bar{1}]$ and $[\bar{1}1\bar{1}]$); see Appendix D. The strength of the magnetic field at the sample distance is around 1 mT. The MW signal is applied with a wire placed on top of the sample with no physical contact. Due to $^{14}$N nuclear spin in this sample, each transition from $m_s = 0 \leftrightarrow m_s = \pm 1$ has three hyperfine components; see Appendix B. Addressing all of these hyperfine splittings simultaneously increases the ODMR contrast [33]. Having the MW resonant with both $m_s = 0 \leftrightarrow m_s = \pm 1$ also increases the ODMR contrast; see Appendix D. Therefore, a set of radiofrequency components is implemented to address all the hyperfine and both electronic state transitions; see Fig. 1(c). The MW signal is generated at the frequency of $f_{\mathrm{SG}_1}$, which is set at the zero-field splitting (ZFS) of the $^3A_2$ ($f_{\mathrm{SG}_1} = f_{\mathrm{ZFS}}$). A second signal generator producing a customized sine wave at three frequencies is mixed with the output signal of the MW signal generator producing six components around the ZFS. The frequencies are adjusted to drive all hyperfine transitions for both spin state transitions. This signal is then amplified and applied to the wire placed on the sample; see Appendix E for more details.

## III. RESULTS AND DISCUSSIONS

In order to measure the pump-induced absorption of the IR probe by the singlet transition, we measured the transmitted beam intensity in two cases: where the sample is pumped (singlet absorption appears) and not pumped (steady state, no singlet absorption). It is expected that the transmitted IR intensity decreases as the pump intensity increases due to absorption by the singlet transition as the $^1E$ level is populated [26,27,34]. However, we also noticed a competing process whereby, upon increasing the pump power, the transmission of the IR probe increases [see inset in Fig. 2(a)]. This is presumably due to the absorption by other defects in the sample that absorb less (i.e., bleach) when excited by the pump. Interestingly, this additional competing process occurs only in our CVD-grown samples and not in high-pressure high-temperature (HPHT) diamond. IR absorption measurements reveal a pronounced zero-phonon line at 1358 nm in the CVD samples that is accompanied by a broad phonon sideband stretching to the singlet absorption region at 1042 nm; see Fig. 2(a). This defect is presumed to be related to hydrogen defects

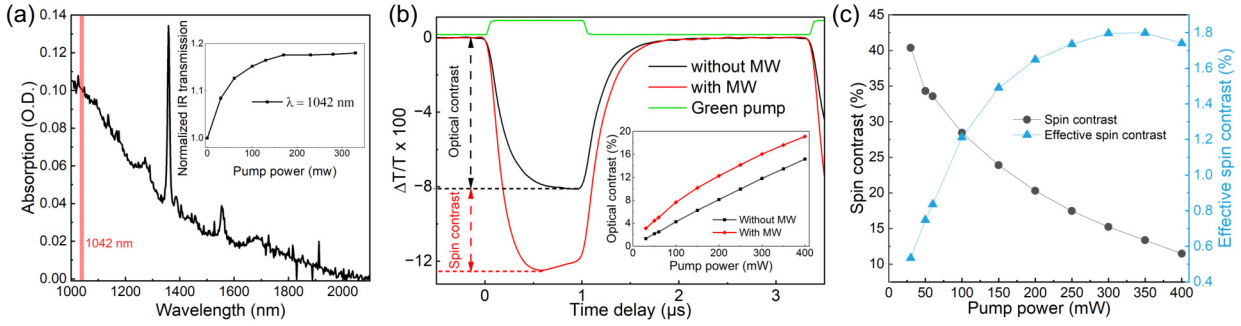


FIG. 2. (a) Absorption spectrum of the sample in the infrared (IR) region. The normalized transmission of the IR beam at 1042 nm for various continuous-wave (CW) pump powers is plotted in the inset. (b) Differential transmission ($\Delta T/T$) at 1042 nm with and without applied MW (red and black curves, respectively). The green plot shows when the pump is on and off. Inset: optical contrast for various pump powers. (c) Spin contrast and effective spin contrast for various pump powers.

and predominantly occurs in CVD diamond [35,36]. It is conceivable that the inevitable coexcitation of this additional defect during a magnetometry measurement has a detrimental effect on the N-$V$ spin relaxation properties, which could potentially favor HPHT diamond over CVD diamond in certain scenarios. It would thus be interesting for future studies to investigate this further.

In order to quantify the absorption of the IR beam due to singlet-level absorption only, that is, to correct for the pump-induced bleaching of the 1358-nm defect absorption, a pulsed pump transient absorption technique was used [34]. Here, the pump power is modulated with the AOM at 300 kHz with a duty cycle of 30%, and the probe transmission of the sample is recorded on the oscilloscope after a transimpedance amplification stage of the photodiode output current. The differential transmission plot of the sample at 1042 nm with and without applied MW is shown in Fig. 2(b). We define *optical contrast* as the maximum differential transmission modulation $\Delta T/T$, which as expected increases almost linearly with pump power [shown in the inset of Fig. 2(b)]. The optical contrast without MW ($C_{\mathrm{noMW}}$) is 8% in Fig. 2(b), whereas maximum $\Delta T/T$ is about 12% with MW ($C_{\mathrm{MW}}$). The contrast between these two values then determines the *spin contrast*, as defined by $(C_{\mathrm{MW}} - C_{\mathrm{noMW}})/(C_{\mathrm{MW}} + C_{\mathrm{noMW}})$. In PL ODMR, all detected N-$V$-PL emissions (not counting possible N-$V^0$ emissions) contribute to the ODMR signal, making the optical contrast essentially 100%. However, this is not the case for absorption ODMR, where the signal will be determined by the product between optical and spin contrast, which we define as the *effective spin contrast* $C_{\mathrm{CW}}$. The power dependence of both spin contrast and effective spin contrast is shown in Fig. 2(c). Note that the pulsed pump scheme is only used to measure the transient absorption signal, whereas all magnetometry measurements are based on CW pumping. To perform absorption ODMR, we CW-pump the sample and measure the transmission of the IR beam while scanning the MW signal across the resonances, shown in Fig. 3(a) for a pump power of 200 mW and an applied bias magnetic field. The peaks are fitted with six Lorentzian functions; see Appendix D for more details. In this case, only the output of signal generator 1 (at $f_{\mathrm{SG_1}}$) is connected to the rf amplifier [bypassing the mixer, shown in Fig. 1(c)]. In Fig. 3(b), the mixed MW signal is applied to address all hyperfine and both $m_s = 0 \leftrightarrow m_s = \pm 1$ transitions. Here, $f_{\mathrm{SG_1}}$ is fixed at the ZFS, 2.870 GHz, and $f_{\mathrm{SG_2}}$ is scanned around 17 MHz. In this case, the central peak has the highest effective spin contrast $C_{\mathrm{CW}} = 1.6\%$ with a FWHM, $\Delta\nu$, of 700 kHz.

To measure the magnetic field, the MW signal is modulated around the central peak frequency $f_{\mathrm{SG_2}}$ with a modulation frequency of $f_{\mathrm{mod}} = 5.6$ kHz and a deviation amplitude of $f_{\mathrm{dev}} = 330$ kHz sweeping the signal generator frequency according to $f_{\mathrm{dev}} \sin(2\pi f_{\mathrm{mod}} t)$. By demodulating the transmitted IR signal using the LIA at the frequency of $f_{\mathrm{mod}}$, we obtain a set of dispersive resonances shown in Fig. 3(c). At the zero-crossing of this curve, the LIA output signal is linear in the difference between the central MW and the magnetic resonance frequency, $S_{\mathrm{LIA}} \sim \alpha(f_c - f_{\mathrm{res}})$, for a small deviation of $|f_c - f_{\mathrm{res}}| \ll \Delta\nu/2$ with the coefficient $\alpha \propto C/\Delta\nu$. This linear response at zero-crossing is fitted with the red line in Fig. 3(c). Small changes in magnetic field are proportional to the LIA output signal and the magnetic field is then calculated by the equation $\Delta B_{\mathrm{N}\text{-}V} = S_{\mathrm{LIA}} h/(g_e \mu_B \alpha \cos(\theta))$, where $\theta$ is the angle between the measured magnetic field (along [110]) and two N-$V$ axes with equal field projection (along [111] and $[\overline{1}11]$), which is equal to 35.3°; see Appendix D for more details.

The magnetic field sensitivity, measured in an unshielded environment in the laboratory, is shown in Fig. 4. It is calculated using the linear spectral density (LSD) of the recorded signal (magnetic field) in time; see Appendix F for details. The data plotted in Fig. 4 is the average LSD of 60 one-second segments of recorded data.

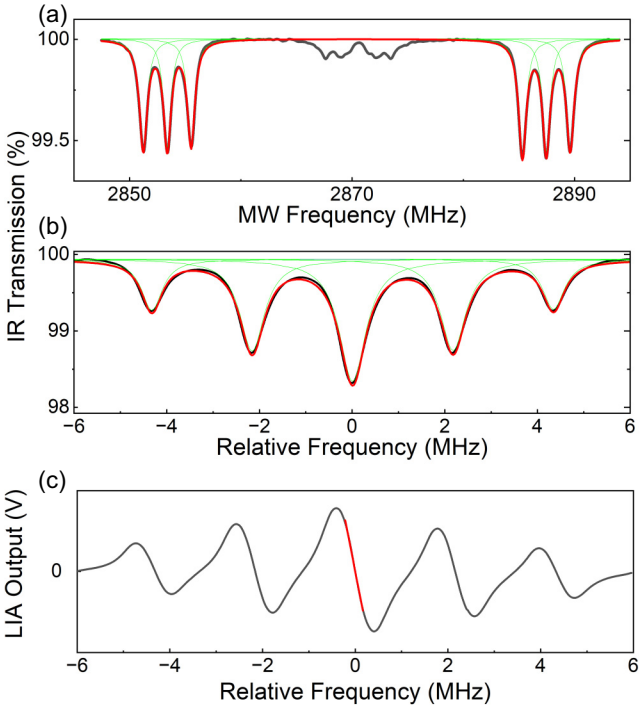


FIG. 3. ODMR plots measured by IR transmission while MW field is scanned. (a) A single MW source is used (SG1). (b) The mixed MW signal addressing all hyperfine splittings for $m_s = 0 \leftrightarrow m_s = \pm 1$. In both cases the black curve is the recorded data, green plots indicate Lorentzian functions fitting an individual peak, and the red plot is the cumulative peaks of the fitting; see Appendix D for more details. (c) The demodulated output of LIA when the MW field is modulated. The red curve shows the fitting of the zero-crossing signal with a line. A bias magnetic field along [110] is applied with a strength of around 1 mT at the sample.

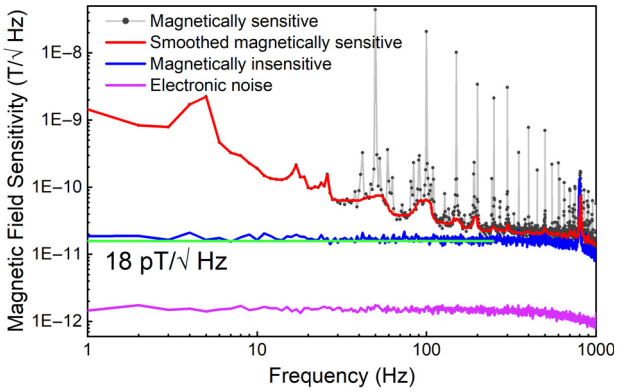


FIG. 4. Relative amplitude spectra of the sensor to characterize the magnetic field sensitivity. It is plotted for magnetically sensitive (black and smoothed curve in red) and magnetically insensitive cases, and electronic noise. The sensitivity noise floor of 18 pT/$\sqrt{\text{Hz}}$ is also shown as a green line.

The sensitivity is plotted for three cases: magnetically sensitive, magnetically insensitive, and electronic noise. In order to obtain the magnetically sensitive case, the MW is applied at the resonance, and all present magnetic fields, including the 50-Hz power line and its higher harmonics, are visible in the measurement. Because of magnetic laboratory interference in the magnetically sensitive curve, it is smoothed with a moving median filter for better illustration (red plot). For the magnetically insensitive measurement, the MW signal is applied far from the resonances, having no effect on the spin of the ground-state electrons. In this case, all nonmagnetic noise sources including laser fluctuations contribute which leads to a sensitivity noise floor of 18 pT/$\sqrt{\text{Hz}}$, representing the lowest value reported so far using IR absorption N-$V$-based magnetometers. Finally, the electronic noise is measured by blocking all the light sources, reaching the noise floor of 1.5 pT/$\sqrt{\text{Hz}}$. The bandwidth (BW) of the magnetic field measurement is defined by the lowpass filter of the LIA, which is set to 1 kHz. The magnetic field sensitivity of the setup is further measured using a test magnetic field; see Appendix H. Based on the measured parameters, the shot-noise sensitivity is calculated to be around 5 pT/$\sqrt{\text{Hz}}$; see Appendix G.

## IV. CONCLUSION

In this paper, we demonstrated a magnetometer that employs ODMR detected via absorption of the IR singlet transition in N-$V^-$ centers at room temperature and without cavity enhancement, achieving a sensitivity of 18 pT/$\sqrt{\text{Hz}}$ from dc to 900 Hz, the lowest value reported so far using singlet absorption ODMR. The absence of a cavity simplifies the setup as it disposes of the need for elaborate cavity stabilization schemes. An additional diamond defect was identified in CVD-grown samples that absorbs in the IR probing range, which may be a limiting factor for further development due to the additional probe-light absorption. Substituting CVD diamond with HPHT diamond could therefore be a sensible choice when building IR absorption ODMR magnetometers or finding ways to remove the defect by suitable material treatment.

There are several avenues for pushing the sensitivity further. The most promising is to increase the probe absorption, and thus the optical contrast, in a multipath (e.g., cavity) beam propagation geometry, which would, however, require incorporating schemes for cavity stabilization. Recent theoretical considerations anticipate sub-picotesla sensitivities using cavities [37]. Pump power stabilization and introducing magnetic shielding should reduce the influence of technical noise, pushing the sensitivity closer to the shot-noise limit, which in turn could be decreased even further by increasing the IR probe power. Pulsed ODMR approaches would provide another path for improvement, as potentially do magnetic flux concentrators [38].

## ACKNOWLEDGMENTS

We acknowledge Marc-Jan van Zadel and Florian Gericke for technical support and Mahsa Ebrahimi for help with preliminary experiments. We acknowledge funding by the Max-Planck Society. We also acknowledge support from the European Commission's Horizon Europe Framework Program under Research and Innovation Action MUQUABIS Grant Agreement No. 101070546; by the Deutsche Forschungsgemeinschaft (DFG, German Research Foundation) in the framework to the collaborative research center "Defects and Defect Engineering in Soft Matter" (SFB1552) under Project No. 465145163; by the Carl-Zeiss-Stiftung (HYMMS P2022-03-044); and by the German Federal Ministry of Education and Research (BMBF) within the Quantumtechnologien program through the DIAQNOS project (project no. 13N16455).

## DATA AVAILABILITY

The data that support the findings of this paper are openly available [39].

## APPENDIX A: ABSORPTION SPECTRUM OF THE SAMPLE

The sample is a $^{12}$C-enriched CVD-grown bulk diamond (Element Six). The nitrogen concentration of the sample before N-$V$ creation is 13 ppm. The N-$V$ concentration including both charge states is approximately 4 ppm. The absorption spectrum of the sample with a thickness of 0.5 mm is shown in Fig. 5.

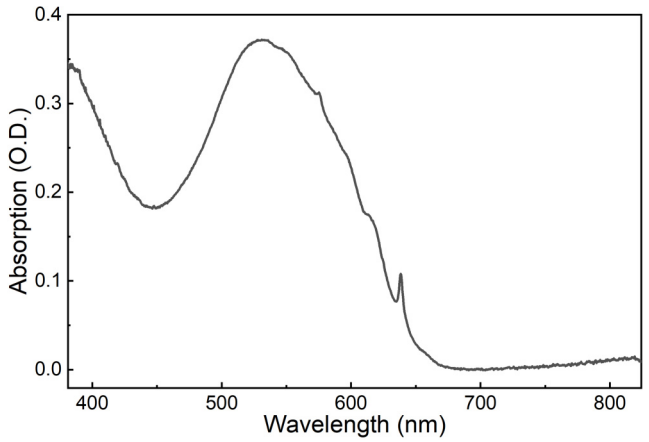


FIG. 5. The absorption spectrum of the sample. The zero-phonon line (ZPL) of N-$V^-$ at 637 nm and its phonon sideband (PSB) on the blue side is visible. Some amount of neutrally charged N-$V$ (N-$V^0$) can also be identified, recognizable by the ZPL peak at 575 nm.

## APPENDIX B: GROUND TRIPLET STATE $^3A_2$ IN N-$V^-$

The N-$V^-$ ground state , $^3A_2$, is an electronic spin-triplet state with $m_s = 0, \pm 1$. The $m_s = \pm 1$ states are degenerate at zero magnetic fields and lie above $m_s = 0$ with energy 2.87 GHz, which is the zero-field splitting (ZFS). By applying a magnetic field, the $m_s = -1$ and $+1$ energy levels split in proportion to the applied magnetic field (Zeeman splitting). In this case, the transition frequencies from $m_s = 0$ to $m_s = \pm 1$ are given by the equation

$$\nu_\pm = D \pm \frac{g_e \mu_B}{h} B_{\text{N-}V} \tag{B1}$$

where $D$ is the zero field splitting, $g_e \approx 2$ is the electronic $g$ factor, $\mu_B$ is the Bohr magneton, $h$ is Planck's constant, and $B_{\text{N-}V}$ is the projection of the magnetic field onto the N-$V$ axis [3]. Because of the four orientations of N-$V$ along [111], [$\bar{1}\bar{1}$1], [1$\bar{1}\bar{1}$], and [$\bar{1}$1$\bar{1}$], there will be separate splitting for each axis depending on the magnetic field's projection along them.

In addition to the Zeeman splitting in the ground state, nuclear spins result in hyperfine splitting. In this case, the energy level of the N-$V$ center experiences hyperfine splitting due to the nuclear spin of the nitrogen atom, where it can be $^{14}$N or $^{15}$N, which are spin-1 and spin-$\frac{1}{2}$ systems, respectively. The sample used here is $^{12}$C-enriched, which eliminates the $^{13}$C nuclear spin contribution. The nitrogen defects are $^{14}$N, resulting in three states for each electronic spin. The $^{14}$N hyperfine splitting is 2.16 MHz [40] and the resulting splitting in the ground triplet state of N-$V^-$ is shown in Fig. 6.

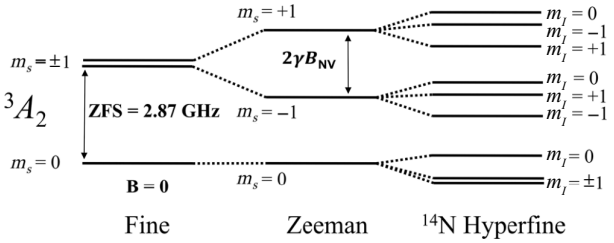


FIG. 6. Ground triplet electronic structure of N-$V^-$ with Zeeman splitting and $^{14}$N hyperfine structure due to nitrogen nuclear spin. $\gamma = 2g_e\mu_B/h$ is the gyromagnetic ratio for the N-$V$ center.

## APPENDIX C: TRANSITION RATES IN N-$V^-$

As shown in the schematic of N-$V^-$ in Fig. 7, by pumping the sample, the excited electrons have two relaxation paths. They either relax down to the ground triplet state by photoluminescence (PL), or by the nonradiative channel through the singlet states ($^3E \rightarrow {}^1A_1 \rightarrow {}^1E \rightarrow {}^3A_2$) via intersystem crossings (ISCs). The PL and ISC rates are spin-dependent. Electrons with spin $m_s = \pm 1$ tend to have a higher probability of having an ISC than the $m_s = 0$ state [1]. In order to quantify the spin contrast, the transition rates for the six-level system N-$V$ that is sketched in Fig. 7 are listed in Table I. Given the parameters in the table, the spin selectivity of ISC and PL is noticeable in the different rates of ISC and PL from $m_s = 0$ and $m_s = \pm 1$. By comparing their values, it can be concluded that the ISC-involved process (i.e., IR transition) has a higher spin contrast due to higher spin selectivity in the ISC path. The spin selectivity for PL detection from $m_s = 0$ is calculated to be around 44%, while for the ISC-involved process from $m_s = \pm 1$ it is approximately 89%. These values are calculated assuming an equal electron population in all $m_s = 0$ and $m_s = \pm 1$ of the excited state $^3E$, followed by relaxation with the rates listed below.

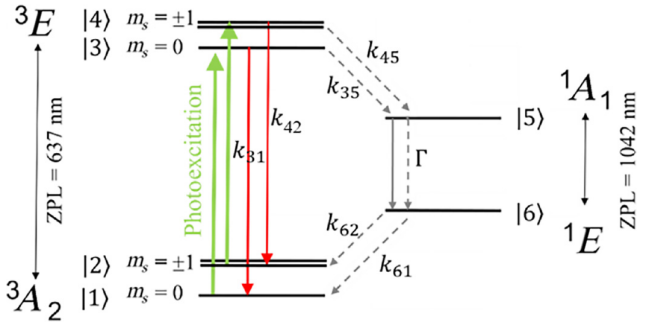


FIG. 7. Schematic of N-$V^-$ with the transition rates shown on each arrow $k_{ij}$.

TABLE I. The transition rates for the six-level N-$V^-$ system sketched in Fig. 7. The $k_{ij}$ parameters are taken from [41]. $1/\Gamma$ is the lifetime of upper singlet, $^1A_1$, taken from [18].

| Parameter | Value |
|---|---|
| $k_{42} = k_{31}$ | $(66 \pm 5)\ \mu s^{-1}$ |
| $k_{35}$ | $(7.9 \pm 4.1)\ \mu s^{-1}$ |
| $k_{45}$ | $(53 \pm 7)\ \mu s^{-1}$ |
| $k_{61}$ | $(1.0 \pm 0.8)\ \mu s^{-1}$ |
| $k_{62}$ | $(0.7 \pm 0.5)\ \mu s^{-1}$ |
| $\Gamma$ | $10\ ns^{-1}$ |

TABLE II. Fitting parameters of the CW ODMR graph shown in Fig. 3(a) with six Lorentzian functions.

| Peak index | FWHM (MHz) | Contrast (%) | Central frequency (MHz) |
|---|---|---|---|
| 1 | 0.85 | −0.54 | 2851.23 |
| 2 | 0.82 | −0.53 | 2853.39 |
| 3 | 0.80 | −0.52 | 2855.53 |
| 4 | 0.83 | −0.58 | 2885.32 |
| 5 | 0.84 | −0.55 | 2887.46 |
| 6 | 0.84 | −0.54 | 2889.61 |

## APPENDIX D: ODMR USING IR ABSORPTION

To perform absorption ODMR, we CW-pump the sample and measure the transmission of the IR beam while scanning the MW signal across the resonances. Because of the four possible orientations of N-$V$ in the crystal, each may have a different projection of the applied magnetic field along their axes. The ODMR plot in a case where the applied magnetic field has different projections on each N-$V$ axis is shown in Fig. 8 (black curve). In this case, the different projections cause different Zeeman splittings for each N-$V$ orientation. Each splitting also has three peaks due to the hyperfine splitting of $^{14}$N. Because of the preferred polarization dependent on the optical beams and the MW source, two pairs of peaks have higher intensity than the other two. By aligning the applied magnetic field along the [110] orientation, the projections of the magnetic field on two N-$V$ axes ([111] and $[\bar{1}\bar{1}1]$) are equal, and the angle between them is 35.3°, and the angle with the other two axes ($[1\bar{1}\bar{1}]$ and $[\bar{1}1\bar{1}]$) is 90°. This bias field orientation creates two pairs of overlapping N-$V$ axes, shown in Fig. 8 (red curve).

The graph with two pairs of peaks, which is illustrated in Fig. 3(a), is fitted with six Lorentzian functions and the fitting parameters are listed in Table II. The contrast is the intensity of the ODMR peak for a single hyperfine splitting in the normalized IR transmission graph.

The ODMR measurements were performed for various pump and MW powers, and the ratio of the contrast and FWHM for a single ODMR peak was calculated to find the optimum powers. The contrast to FWHM ratio for a single peak [e.g., a single hyperfine transition plotted in Fig. 3(a)] for various pump powers is plotted in Fig. 9. The parameters for a fixed pump power and various MW powers are plotted in Fig. 10. The $x$ axis is the MW power that is applied to the input of the MW amplifier (with a gain of 46 dB).

Driving the hyperfine transitions at the same time increases the contrast to FWHM ratio, thus the magnetic sensitivity. Besides, addressing both transitions for $m_s = 0 \leftrightarrow m_s = +1$ and $m_s = 0 \leftrightarrow m_s = -1$ further increases the ratio. Therefore, with the MW mixing technique, we drive all hyperfine transitions for N-$V$ oriented along [111] and $[\bar{1}\bar{1}1]$. In this case, the ODMR plot has five peaks as shown in Fig. 3(b), which is fitted with five Lorentzian peaks with the parameters listed in Table III.

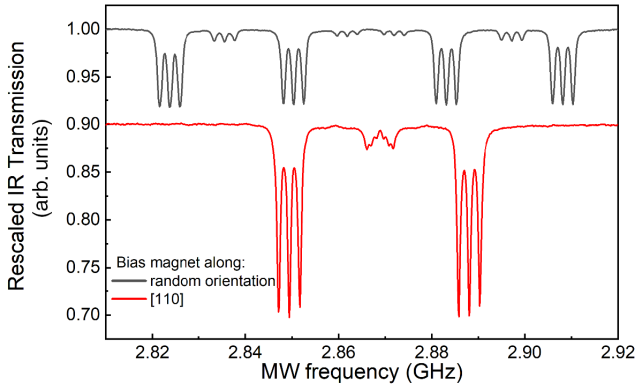


FIG. 8. The ODMR graph when a bias magnetic field is applied at a random orientation, creating different magnetic field projections on each N-$V$ axis (black curve) and when it is applied along [110], creating two pairs of peaks (red curve). The dc level of the red curve is shifted for better illustration.

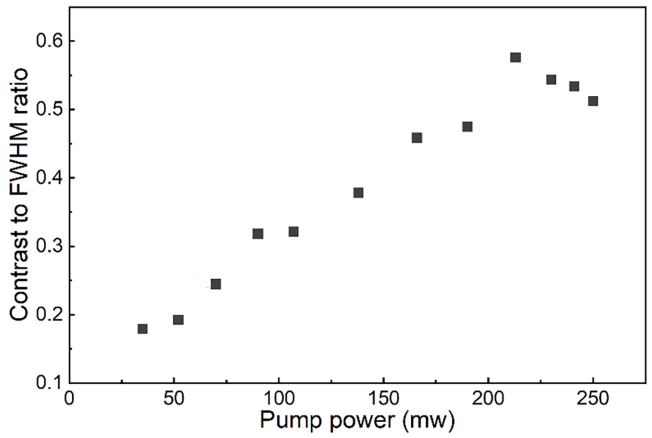


FIG. 9. CW ODMR contrast to FWHM ratio for various pump powers.

TABLE III. Fitting parameters of the CW ODMR when exciting all hyperfine splitting, which creates five peaks, shown in Fig. 3(b).

| Peak index | FWHM (MHz) | Contrast (%) | Central frequency (MHz) |
|---|---|---|---|
| 1 | 0.55 | −0.67 | −4.32 |
| 2 | 0.65 | −1.20 | −2.16 |
| 3 | 0.70 | −1.60 | 0.01 |
| 4 | 0.67 | −1.19 | 2.18 |
| 5 | 0.57 | −0.65 | 4.35 |

The MW power is scanned to find the optimum power while addressing all the hyperfine transitions. The contrast, FWHM, and their ratio are plotted in Fig. 11. The $x$-axis is the power of the MW signal generator (SG1) that is then mixed with the output of the other signal generator (SG2) using a mixer. The MW power before the MW amplifier was measured using an oscilloscope, which for 8 dBm input power results in −22 dBm for each peak intensity. The total MW power at the input of the MW amplifier is −14 dBm.

## APPENDIX E: MICROWAVE DELIVERY SYSTEM

The rf system to apply the MW includes a MW signal generator SG1 (SG396 Stanford Research Systems), a custom sine wave generator, SG2 (a homemade VHDL code to run on the field-programmable gate array board of Moku:Pro, Liquid Instruments), an rf mixer (ZX05-U4324H-S+, Mini-Circuits), an rf amplifier (ZHL-15W-422X-S+, Mini-Circuits), and a circulator terminated with a 50-ohm resistor (UIYBCC6434A2T4SF, UIY). To drive all hyperfine transitions, SG1 generates a sine wave at the central frequency of the zero-field splitting (ZFS), $f_{\mathrm{SG1}} = f_{\mathrm{ZFS}} = 2.87$ GHz. SG2 generates three sine waves with a central frequency of $f_c$ and sidebands at $f_c \pm 2.16$ MHz. $f_c$ is adjusted to be equal to the Zeeman splitting of the $m_s = \pm 1$ states, $f_c = g_e \mu_B B_{N-V}$, and 2.16 MHz is the hyperfine splitting energy due to $^{14}$N. The output of SG1 is connected to the local oscillator (LO) of the mixer and the SG2 output is connected to the intermediate frequency pin (IF). The output of the mixer is given by

$$\begin{aligned} S_{\mathrm{Applied}} = &\sin\left(2\pi\left(f_{\mathrm{ZFS}} + f_c\right)t\right) \\ &+ \sin\left(2\pi\left(f_{\mathrm{ZFS}} + f_c + 2.16\ \mathrm{MHz}\right)t\right) \\ &+ \sin\left(2\pi\left(f_{\mathrm{ZFS}} + f_c - 2.16\ \mathrm{MHz}\right)t\right) \\ &+ \sin\left(2\pi\left(f_{\mathrm{ZFS}} - f_c\right)t\right) \\ &+ \sin\left(2\pi\left(f_{\mathrm{ZFS}} - f_c - 2.16\ \mathrm{MHz}\right)t\right) \\ &+ \sin\left(2\pi\left(f_{\mathrm{ZFS}} - f_c + 2.16\ \mathrm{MHz}\right)t\right). \end{aligned} \tag{E1}$$

This signal is then connected to the rf amplifier, whose output is connected to the circulator. The output of the circulator is connected to a closed-loop wire placed on top of the sample with no physical contact. The Fourier transform of the MW signal applied to the amplifier is measured using an oscilloscope and plotted in Fig. 12.

For magnetometry measurement, which is explained in the main text, the frequency of SG2 output is modulated with a modulation frequency of $f_{\mathrm{mod}}$ and deviation amplitude of $f_{\mathrm{dev}}$. In this case, the input signal of the amplifier is given by

$$\begin{aligned} S_{\mathrm{Applied}} = &\sin\left(2\pi\left(f_{\mathrm{ZFS}} + f_c\right)t + f_{\mathrm{dev}}\sin(2\pi f_{\mathrm{mod}}t)\right) \\ &+ \sin\left(2\pi\left(f_{\mathrm{ZFS}} + f_c + 2.16\ \mathrm{MHz}\right)t\right. \\ &\left.+ f_{\mathrm{dev}}\sin(2\pi f_{\mathrm{mod}}t)\right) \\ &+ \sin\left(2\pi\left(f_{\mathrm{ZFS}} + f_c - 2.16\ \mathrm{MHz}\right)t\right. \\ &\left.+ f_{\mathrm{dev}}\sin(2\pi f_{\mathrm{mod}}t)\right) \\ &+ \sin\left(2\pi\left(f_{\mathrm{ZFS}} - f_c\right)t - f_{\mathrm{dev}}\sin(2\pi f_{\mathrm{mod}}t)\right) \\ &+ \sin\left(2\pi\left(f_{\mathrm{ZFS}} - f_c - 2.16\ \mathrm{MHz}\right)t\right. \\ &\left.- f_{\mathrm{dev}}\sin(2\pi f_{\mathrm{mod}}t)\right) \\ &+ \sin\left(2\pi\left(f_{\mathrm{ZFS}} - f_c + 2.16\ \mathrm{MHz}\right)t\right. \\ &\left.- f_{\mathrm{dev}}\sin(2\pi f_{\mathrm{mod}}t)\right). \end{aligned} \tag{E2}$$

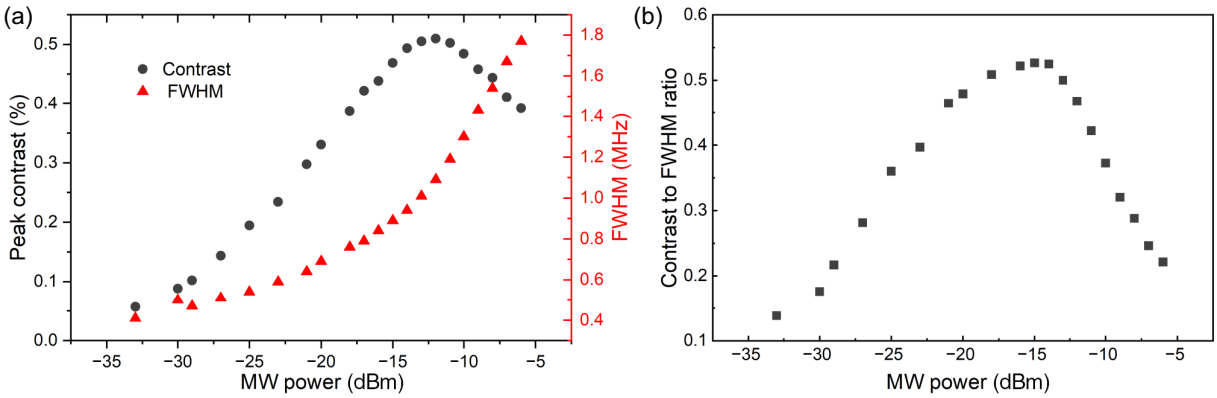


FIG. 10. The CW ODMR (a) contrast and FWHM and (b) their ratio for peak number 2 (listed in Table II) for various MW powers.

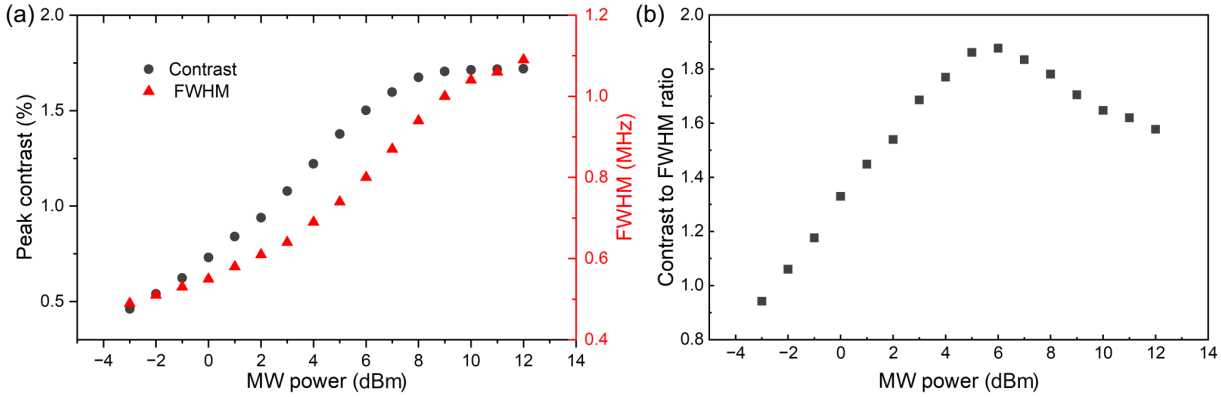


FIG. 11. The CW ODMR (a) contrast and FWHM and (b) their ratio for peak number 3 (listed in Table III) for various MW powers. This is the case when all the hyperfine levels for both $m_s = \pm 1$ are driven by the MW signal.

## APPENDIX F: SENSITIVITY CALCULATION

To calculate the sensitivity graph, the LIA output, which is demodulated at the $f_{\text{mod}}$, is first recorded for 60 s and is converted to the magnetic field with the conversion ratio. Then the data are split into 60 one-second-long measurements and the power spectral density for each 1-second segment is calculated. This is achieved by calculating the square root of the Fourier transform, which results in the linear spectral density (LSD). Finally, all of the spectral density curves are averaged together, which gives the sensitivity graph shown in Fig. 4. The reason for splitting the data into 1-second segments is that the LSD might have a different value than the linear spectrum (LS) that determines the root square mean (rms). The LSD and LS conversion ratio is given by

$$\text{LSD} = \frac{LS}{\sqrt{ENBW}} \tag{F1}$$

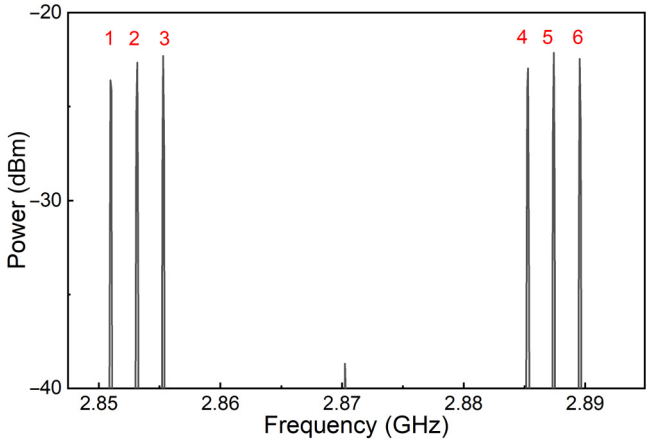


FIG. 12. The power spectrum of the applied MW signal to the amplifier at six frequencies addressing all hyperfine states for both $m_s = 0 \leftrightarrow m_s = \pm 1$.

where ENBW is effective noise bandwidth, which is given by

$$\text{ENBW} = \text{NENBW} \cdot \frac{f_s}{N}, \tag{F2}$$

and NENBW is the normalized equivalent noise bandwidth, $f_s$ is the sampling frequency, and $N$ is the number of data points. The NENBW depends on the window function used in the calculation of the Fourier transform. The rectangular window function utilized in this case has an NENBW value of 1. Given the equations, if $f_s = N$, the linear spectral density is equal to the linear spectrum. Therefore, the measured magnetic field LSD has the same value as the rms value of the applied field at the specified frequency.

## APPENDIX G: SHOT-NOISE SENSITIVITY CALCULATIONS

To calculate the shot-noise sensitivity for CW ODMR, we use

$$\eta_{\text{CW}} = \frac{4}{3\sqrt{3}} \frac{h}{g_e \mu_B} \frac{\Delta\nu}{C_{\text{CW}}\sqrt{R}} \tag{G1}$$

where $h$ is Planck's constant, $g_e$ is the N-$V$ electronic $g$ factor, $\mu_B$ is the Bohr magneton, $\Delta\nu$ and $C_{\text{CW}}$ are the linewidth and the contrast of the ODMR peak respectively, and $R$ is the photon-detection rate [3]. In our measurements, by driving all the hyperfine splitting transitions simultaneously for $m_s = 0 \leftrightarrow m_s = \pm 1$, a contrast of $C_{\text{CW}} = 1.6\%$ and a linewidth of $\Delta\nu = 0.7$ MHz are achieved. Here, $R$ is calculated from the power of the detected IR on the photodiode, which is around 12 mW. These parameters result in an estimated shot-noise

sensitivity of around

$$\eta_{\mathrm{CW}} = 5\ \mathrm{pT}/\sqrt{\mathrm{Hz}}. \tag{G2}$$

Given the sensitivity noise floor of 18 $\mathrm{pT}/\sqrt{\mathrm{Hz}}$, further sensitivity improvements are possible. Furthermore, given that the shot-noise limit in this technique is determined by the external IR light source power, it can be further reduced by increasing the IR power.

## APPENDIX H: CALIBRATING THE MAGNETIC FIELD SENSOR

As previously outlined in this chapter, the output signal of the LIA can be converted to the magnetic field by multiplying with a coefficient. In order to ensure that the measured magnetic field is correct, we also perform a test measurement with a known magnetic field. The magnetic field is applied along [110] by a homemade coil with a radius of $r = 20$ mm, $N = 10$ turns, and placed at a distance of about $d = 26$ mm from the sample. The coil is connected to a signal generator in series with a 1-kΩ resistor. The magnetic field generated by the coil is given by

$$B_{\mathrm{rms}} = \frac{\mu_0 I_{\mathrm{rms}} N}{2} \frac{r^2}{(r^2 + d^2)^{3/2}} \tag{H1}$$

where $I_{\mathrm{rms}}$ is given by the rms applied voltage ($V_{\mathrm{rms}}$) divided by the 1-kΩ resistance in series. First, 10-V peak-peak square pulses are applied to the coil at a frequency of 1 Hz. The LIA output and the corresponding calculated magnetic field are plotted in Fig. 13. The calculated applied magnetic field from the equation mentioned above is 0.71 μT, and the measured parameter (shown in Fig. 13), is 0.69 μT, which is within a 3% error bar.

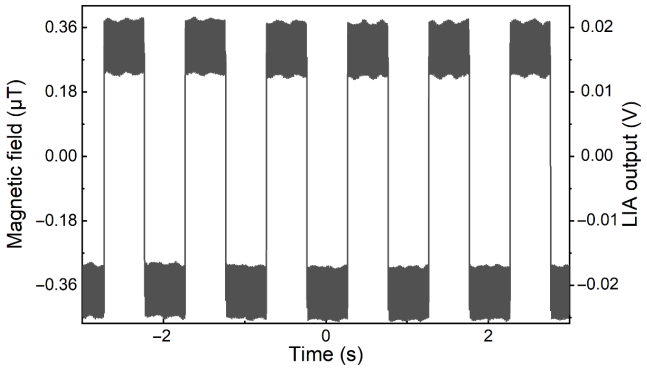


FIG. 13. Applied test field with a peak-to-peak intensity of 0.71 μT with a frequency of 1 Hz measured with the sensor and the output voltage of the LIA is plotted.

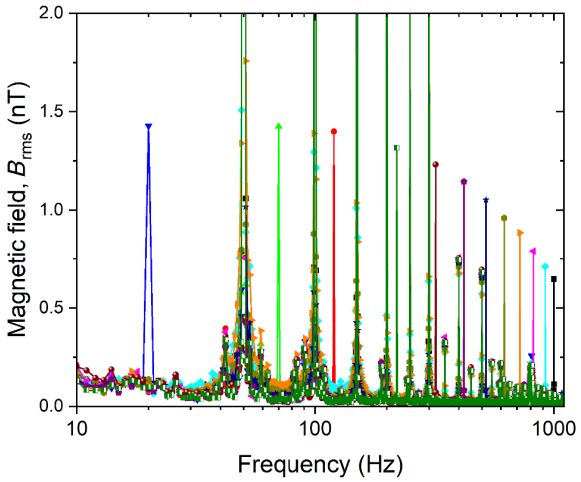


FIG. 14. Magnetic field spectrum when sinusoidal test magnetic fields are applied at various frequencies. The peaks at 50 Hz and its higher harmonics are due to the line power magnetic noise in the laboratory.

For further testing of the magnetic sensor, ac magnetic fields at different frequencies are applied to the sample in the frequency range from 20 to 1000 Hz, as illustrated in Fig. 14. The measured values at these frequencies are listed in Table IV. As shown, the measured value decreases as the frequency increases. The magnetic field intensity calculated by the coil equation is 1.40 nT (20 $\mathrm{mV_{rms}}$ applied to the coil). Therefore, a calibration factor is required for the sensor to operate at various frequencies. The calibration factor is shown in Fig. 15. The measured value with the sensor must be multiplied by the calibration factor to calculate the applied magnetic field. This frequency-dependent behavior is believed to be due to the integration time constant of the lock-in amplifier.

TABLE IV. Measured test magnetic field value at various frequencies.

| Frequency (Hz) | Measured $B_{\mathrm{rms}}$ (nT) |
|---|---|
| 20 | 1.42 |
| 70 | 1.42 |
| 120 | 1.40 |
| 220 | 1.31 |
| 320 | 1.23 |
| 420 | 1.14 |
| 520 | 1.05 |
| 620 | 0.96 |
| 820 | 0.88 |
| 820 | 0.79 |
| 920 | 0.71 |
| 1000 | 0.65 |

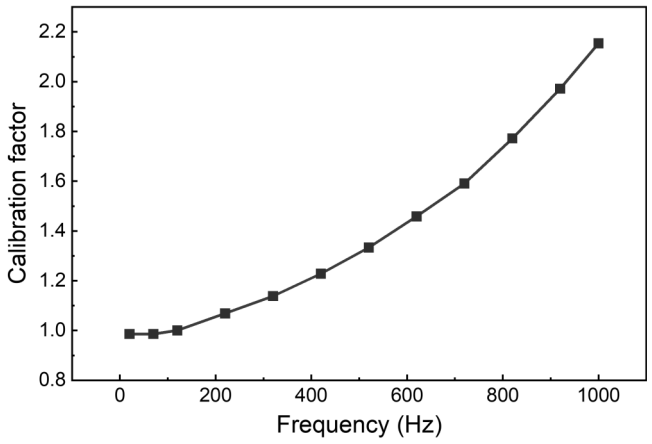


FIG. 15. Calibration factor calculated based on the test magnetic field to calibrate the real applied magnetic field value.


[1] M. W. Doherty, N. B. Manson, P. Delaney, F. Jelezko, J. Wrachtrup, and L. C. Hollenberg, The nitrogen-vacancy colour centre in diamond, Phys. Rep. **528**, 1 (2013).

[2] M. Strzałka, D. Kwiatkowski, Ł. Cywiński, and K. Roszak, Qubit-environment negativity versus fidelity of conditional environmental states for a nitrogen-vacancy-center spin qubit interacting with a nuclear environment, Phys. Rev. A **102**, 042602 (2020).

[3] J. F. Barry, J. M. Schloss, E. Bauch, M. J. Turner, C. A. Hart, L. M. Pham, and R. L. Walsworth, Sensitivity optimization for NV-diamond magnetometry, Rev. Mod. Phys. **92**, 015004 (2020).

[4] J. F. Barry, M. H. Steinecker, S. T. Alsid, J. Majumder, L. M. Pham, M. F. O'Keeffe, and D. A. Braje, Sensitive ac and dc magnetometry with nitrogen-vacancy-center ensembles in diamond, Phys. Rev. Appl. **22**, 044069 (2024).

[5] K. Bian, W. Zheng, X. Zeng, X. Chen, R. Stöhr, A. Denisenko, S. Yang, J. Wrachtrup, and Y. Jiang, Nanoscale electric-field imaging based on a quantum sensor and its charge-state control under ambient condition, Nat. Commun. **12**, 2457 (2021).

[6] M. Block, B. Kobrin, A. Jarmola, S. Hsieh, C. Zu, N. Figueroa, V. Acosta, J. Minguzzi, J. Maze, D. Budker, *et al.*, Optically enhanced electric field sensing using nitrogen-vacancy ensembles, Phys. Rev. Appl. **16**, 024024 (2021).

[7] F. Dolde, H. Fedder, M. W. Doherty, T. Nöbauer, F. Rempp, G. Balasubramanian, T. Wolf, F. Reinhard, L. C. Hollenberg, F. Jelezko, *et al.*, Electric-field sensing using single diamond spins, Nat. Phys. **7**, 459 (2011).

[8] P. Ovartchaiyapong, K. W. Lee, B. A. Myers, and A. C. B. Jayich, Dynamic strain-mediated coupling of a single diamond spin to a mechanical resonator, Nat. Commun. **5**, 4429 (2014).

[9] M. E. Trusheim and D. Englund, Wide-field strain imaging with preferentially aligned nitrogen-vacancy centers in polycrystalline diamond, New J. Phys. **18**, 123023 (2016).

[10] G. Kucsko, P. C. Maurer, N. Y. Yao, M. Kubo, H. J. Noh, P. K. Lo, H. Park, and M. D. Lukin, Nanometre-scale thermometry in a living cell, Nature **500**, 54 (2013).

[11] A. M. Wojciechowski, M. Karadas, C. Osterkamp, S. Jankuhn, J. Meijer, F. Jelezko, A. Huck, and U. L. Andersen, Precision temperature sensing in the presence of magnetic field noise and *vice-versa* using nitrogen-vacancy centers in diamond, Appl. Phys. Lett. **113**, 011101 (2018).

[12] F. Casola, T. Van Der Sar, and A. Yacoby, Probing condensed matter physics with magnetometry based on nitrogen-vacancy centres in diamond, Nat. Rev. Mater. **3**, 1 (2018).

[13] J. F. Barry, M. J. Turner, J. M. Schloss, D. R. Glenn, Y. Song, M. D. Lukin, H. Park, and R. L. Walsworth, Optical magnetic detection of single-neuron action potentials using quantum defects in diamond, Proc. Natl. Acad. Sci. **113**, 14133 (2016).

[14] Y. Wu, F. Jelezko, M. B. Plenio, and T. Weil, Diamond quantum devices in biology, Angew. Chem. Int. Ed. **55**, 6586 (2016).

[15] D. R. Glenn, R. R. Fu, P. Kehayias, D. Le Sage, E. A. Lima, B. P. Weiss, and R. L. Walsworth, Micrometer-scale magnetic imaging of geological samples using a quantum diamond microscope, Geochem. Geophys. Geosyst. **18**, 3254 (2017).

[16] D. A. Hopper, H. J. Shulevitz, and L. C. Bassett, Spin readout techniques of the nitrogen-vacancy center in diamond, Micromachines **9**, 437 (2018).

[17] R. Ulbricht, S. Dong, A. Gali, S. Meng, and Z.-H. Loh, Vibrational relaxation dynamics of the nitrogen-vacancy center in diamond, Phys. Rev. B **97**, 220302 (2018).

[18] R. Ulbricht and Z.-H. Loh, Excited-state lifetime of the NV-infrared transition in diamond, Phys. Rev. B **98**, 094309 (2018).

[19] V. Acosta, A. Jarmola, E. Bauch, and D. Budker, Optical properties of the nitrogen-vacancy singlet levels in diamond, Phys. Rev. B—Condens. Matter Mater. Phys. **82**, 201202 (2010).

[20] M. T. Luu, A. T. Younesi, and R. Ulbricht, Nitrogen-vacancy centers in diamond: discovery of additional electronic states, Mater. Quantum Technol. **4**, 035201 (2024).

[21] V. Ivády, H. Zheng, A. Wickenbrock, L. Bougas, G. Chatzidrosos, K. Nakamura, H. Sumiya, T. Ohshima, J. Isoya, D. Budker, *et al.*, Photoluminescence at the ground-state level anticrossing of the nitrogen-vacancy center in diamond: A comprehensive study, Phys. Rev. B **103**, 035307 (2021).

[22] L. Rogers, S. Armstrong, M. Sellars, and N. Manson, Infrared emission of the NV centre in diamond: Zeeman and uniaxial stress studies, New J. Phys. **10**, 103024 (2008).

[23] V. M. Acosta, E. Bauch, M. P. Ledbetter, A. Waxman, L.-S. Bouchard, and D. Budker, Temperature dependence of the nitrogen-vacancy magnetic resonance in diamond, Phys. Rev. Lett. **104**, 070801 (2010).

[24] H. A. El-Ella, S. Ahmadi, A. M. Wojciechowski, A. Huck, and U. L. Andersen, Optimised frequency modulation for continuous-wave optical magnetic resonance sensing using nitrogen-vacancy ensembles, Opt. Express **25**, 14809 (2017).

[25] V. Acosta, E. Bauch, A. Jarmola, L. Zipp, M. Ledbetter, and D. Budker, Broadband magnetometry by infrared-absorption detection of nitrogen-vacancy ensembles in diamond, Appl. Phys. Lett. **97**, 174104 (2010).

[26] K. Jensen, N. Leefer, A. Jarmola, Y. Dumeige, V. M. Acosta, P. Kehayias, B. Patton, and D. Budker, Cavity-enhanced room-temperature magnetometry using absorption by nitrogen-vacancy centers in diamond, Phys. Rev. Lett. **112**, 160802 (2014).

[27] G. Chatzidrosos, A. Wickenbrock, L. Bougas, N. Leefer, T. Wu, K. Jensen, Y. Dumeige, and D. Budker, Miniature cavity-enhanced diamond magnetometer, Phys. Rev. Appl. **8**, 044019 (2017).

[28] L. Bougas, A. Wilzewski, Y. Dumeige, D. Antypas, T. Wu, A. Wickenbrock, E. Bourgeois, M. Nesladek, H. Clevenson, D. Braje, *et al.*, On the possibility of miniature diamond-based magnetometers using waveguide geometries, Micromachines **9**, 276 (2018).

[29] J. M. Bopp, H. Conradi, F. Perona, A. Palaci, J. Wollenberg, T. Flisgen, A. Liero, H. Christopher, N. Keil, W. Knolle, A. Knigge, W. Heinrich, M. Kleinert, and T. Schröder, Diamond-on-chip magnetic field camera for mobile imaging, Phys. Rev. Appl. **23**, 034024 (2025), doi:10.1103/PhysRevApplied.23.034024).

[30] F. Münzhuber, F. Bayer, V. Marković, J. Brehm, J. Kleinlein, L. Molenkamp, and T. Kiessling, Polarization-assisted vector magnetometry with no bias field using an ensemble of nitrogen-vacancy centers in diamond, Phys. Rev. Appl. **14**, 014055 (2020).

[31] S. Ahmadi, H. A. El-Ella, J. O. Hansen, A. Huck, and U. L. Andersen, Pump-enhanced continuous-wave magnetometry using nitrogen-vacancy ensembles, Phys. Rev. Appl. **8**, 034001 (2017).

[32] S. Ahmadi, H. A. El-Ella, A. M. Wojciechowski, T. Gehring, J. O. Hansen, A. Huck, and U. L. Andersen, Nitrogen-vacancy ensemble magnetometry based on pump absorption, Phys. Rev. B **97**, 024105 (2018).

[33] A. K. Dmitriev and A. K. Vershovskii, Concept of a microscale vector magnetic field sensor based on nitrogen-vacancy centers in diamond, J. Opt. Soc. Am. B **33**, B1 (2016), doi:10.1364/JOSAB.33.0000B1).

[34] A. T. Younesi and R. Ulbricht, Broadband transient absorption spectroscopy using an incoherent white-light source as probe, Opt. Express **30**, 38896 (2022).

[35] F. Fuchs, C. Wild, K. Schwarz, W. Müller-Sebert, and P. Koidl, Hydrogen induced vibrational and electronic transitions in chemical vapor deposited diamond, identified by isotopic substitution, Appl. Phys. Lett. **66**, 177 (1995).

[36] A. M. Zaitsev, *Optical Properties of Diamond: A Data Handbook* (Springer Science & Business Media, Berlin, 2013).

[37] H. Zadeh-Haghighi, O. Golami, V. K. Kavatamane, P. E. Barclay, and C. Simon, Master-equation-based model for infrared-based magnetometry with nitrogen-vacancy-centers-in-diamond cavities: A path to subpicotesla sensitivity at submillimeter scales, Phys. Rev. Appl. **22**, 064015 (2024).

[38] Y. Xie, H. Yu, Y. Zhu, X. Qin, X. Rong, C.-K. Duan, and J. Du, A hybrid magnetometer towards femtotesla sensitivity under ambient conditions, Sci. Bull. **66**, 127 (2021).

[39] https://doi.org/10.17617/3.0RD8PI.

[40] S. Felton, A. Edmonds, M. E. Newton, P. Martineau, D. Fisher, D. Twitchen, and J. Baker, Hyperfine interaction in the ground state of the negatively charged nitrogen vacancy center in diamond, Phys. Rev. B—Condens. Matter Mater. Phys. **79**, 075203 (2009).

[41] Y. Dumeige, M. Chipaux, V. Jacques, F. Treussart, J.-F. Roch, T. Debuisschert, V. M. Acosta, A. Jarmola, K. Jensen, P. Kehayias, *et al.*, Magnetometry with nitrogen-vacancy ensembles in diamond based on infrared absorption in a doubly resonant optical cavity, Phys. Rev. B—Condens. Matter Mater. Phys. **87**, 155202 (2013).

*Correction:* The omission of a support statement in the Acknowledgments has been fixed.